LA-UR-05-4973

Approved for public release;
distribution is unlimited.

Title: The Interaction of Melt Control Strategy and Electrode Discontinuities In Vacuum Arc Remelting

Author(s):
Robert M. Aikin Jr. and Philip K. Tubesing
Los Alamos National Laboratory, Los Alamos, NM
Rodney L. Williamson and David K. Melgaard
Sandia National Laboratory, Albuquerque, NM
Joseph. J. Beaman
University of Texas, Austin, TX

Intended for:
Proceedings of the 2005 International Symposium on Liquid Metal Processing, Sept 18-21, 2005,
Santa Fe NM

Form 836 (7/06)

Proceedings of the 2005 International Symposium on Liquid Metal Processing, Santa Fe NM Sept 18-21, 2005,
Ed. P.D. Lee, A. Mitchell, R.L. Williamson, and A.S. Ballantyne, ASM International, Metals Park, OH, pp. 71-82.

The Interaction of Melt Control Strategy and Electrode Discontinuities In Vacuum Arc Remelting

Robert M. Aikin Jr. and Philip K. Tubesing
Los Alamos National Laboratory, Los Alamos, NM

Rodney L. Williamson and David K. Melgaard
Sandia National Laboratory, Albuquerque, NM

Joseph. J. Beaman
University of Texas, Austin, TX

Abstract

To assess the effect of electrode discontinuities and different control strategies on ingot quality, welded stainless steel electrodes were vacuum arc remelted (VAR) using two control strategies. Electrodes of 304 stainless steel were fabricated by circumferentially welding four 152 mm diameter sections together. These electrodes were then VAR melted into a 215 mm crucible using (a) constant melt current or (b) constant melt rate. Because of the shallow depth of the welds and the convex electrode tip profile during melting, the welds melted through before the entire section had melted. This allowed an unmelted portion of the electrode tip to drop into the melt pool, resulting in major melt transients. The sections that dropped ranged from 2.8 kg to 4.6 kg in mass, equivalent to an electrode length of 12% to 20% of the electrode diameter. For the ingot melted under constant current control, the dropped sections quenched and capped the melt pool resulting in significant macroporosity in the ingot. In the ingots melted under constant melt rate, the dropped sections were smaller and the controller applied additional current after the drop to recover the melt rate. In this heat the electrode tips melted in the pool, possibly due to an increase in melting current, resulting in a void free ingot. In both cases the melt transients resulted in a significant disruption to the ingot columnar grain structure.

Introduction

Vacuum arc remelting (VAR) is a process for controlled casting of segregation sensitive and reactive metal alloy ingots. In the VAR process, a cylindrically shaped, alloy electrode is loaded into a water-cooled, copper crucible of the VAR furnace, the furnace is evacuated, and a direct current arc is struck between the electrode (cathode) and some starter material at the bottom of the crucible (anode). The arc heats both the starter material and the electrode tip, eventually melting both. As the electrode tip is melted away, molten metal drips off forming an ingot in the copper crucible. Because the crucible diameter is larger than the electrode diameter, the electrode must be translated downward toward the melt pool to keep the mean distance between the electrode tip and pool surface constant. This distance is called the electrode gap. The objective of VAR is to produce an ingot that is free of macrosegregation, porosity, shrinkage cavities, or other defects associated with uncontrolled solidification during casting.

In normal industrial practice, several process variables are monitored and recorded to evaluate the status of the VAR process. These include arc voltage (V), melting current (I), electrode position (X), drip-short frequency (f_{DS}), furnace pressure (P), and electrode mass (M). Drip-shorts are momentary arc interruptions due to metal drips bridging the electrode gap and contacting the ingot pool surface [1]. The electrode mass is used to estimate the electrode melt rate. However, because of the noise inherent in raw load cell data, simply differentiating the output to obtain an "instantaneous" estimate of melt rate yields extremely noisy results. To address this problem, the load cell data is usually filtered, buffered, and fit using a running linear least squares regression, with the resulting slope being used as the average melt rate over the analysis time.

Under steady-state conditions, applying constant melting power produces a constant melt rate. However, the simple relationship between power and melt rate under steady-state conditions is destroyed by transients in the electrode temperature distribution. Such transients occur at the beginning and end of normal melting. They may also be caused by process upsets, such as pressure fluctuations from electrode contamination.

Another extremely transient situation arises as the melt zone approaches a transverse crack in the electrode. The crack impedes heat flow causing material below the crack to heat up more rapidly than normal while material above the crack remains relatively cold. Under constant power conditions, this leads to an increase in melt rate as the melt zone approaches the crack, followed by a rapid decrease as the melt zone passes through the crack and encounters the cool electrode above the crack. Because of their perturbation to the steady-state thermal profile, crack-initiated melt rate events can lead to large perturbations in the melt rate for standard controllers.

Electrode melt rate is an important parameter in the VAR process. Variations cause transients in the ingot growth rate and mushy zone thermal gradient, a condition conducive to the formation of melt related defects. For example, such transients

have been linked to freckle formation [2,3] in nickel-base superalloys, as well as solidification white spot [4,5] and tree-ring [6,7] formation in Inconel 718. A method of VAR process control capable of controlling the melt rate during transient melting and through common melt rate disturbances could lead to significant improvements in product yields as well as reduce the number of melt related defects in segregation sensitive alloys.

Based on a linearized low order dynamic melt rate model, a feedback melt rate controller was designed to be capable of controlling the melt rate through crack events [8]. A full treatment of the mathematical development underlying the controller has been reported by Beaman, *et al.* [9]. The model was incorporated into a process filter that produces estimates of electrode thermal boundary layer, electrode gap, electrode position, and electrode mass. Estimated values for the thermal boundary layer and electrode gap are used for feedback. The input commands into this controller are desired electrode gap and melt rate, while the output commands from the controller to the furnace are melting current and electrode drive speed.

Several papers have examined control though a crack in the electrode using the melt rate controller described above [10, 11]. This paper examines the effect of electrode discontinuities and different control strategies on ingot quality for ingots made from welded stainless steel electrodes using two strategies: (a) constant melt current or (b) constant melt rate.

Experiments

Two identical electrodes were fabricated by circumferentially welding four sections of 304 stainless steel together. This steel was commercially produced by air melting and then wrought processing to make the 154 mm bar. A schematic of the geometry used for the electrodes is shown in Figure 1(a), while the actual electrode is shown in Figure 1(b). The faces of the sections were machined flat, butted together, and then joined by tungsten inert gas welding around 270° of the electrode circumference. These shallow welds are on the order of 3 mm deep.

As shown in Figure 1, a reduced section with an end grove was machined 46 mm on each side of the center weld. This feature was introduced to assess the influence of a fixturing reduction on the arc behavior. Within the inherent noise in the data, this fixturing reduction did not appear to impact the VAR process. A stainless steel nut was tack-welded to the top edge of each section in order to visually mark the point at which the section was burned off. In practice the arc engulfed the nut and melted it off before the section dropped and as such they were not a useful diagnostic.

Both melts were performed in a small VAR furnace at Los Alamos National Laboratory with a 216 mm diameter by 610 mm deep copper crucible. Because of its small size the control of this furnace is more difficult, and the process reacts much more quickly to process changes, than most commercial sized VAR furnaces.

A plate of 304 stainless 154 mm in diameter by 10 mm tall along with 1.0 kg of stainless nuts were place in the crucible prior to each melt to act as a starter material and aid in strike off. In this small furnace the annulus between the electrode and crucible is 32 mm. This annular distance is not much greater than the electrode gap. If the electrode gap is not kept tight, arc activity is transferred to the electrode sides resulting in a rapid rounding of the electrode tip.

A direct, non-intrusive measurement of electrode gap is not available, so drip-short frequency was measured and the electrode gap was estimated according the following measurement model [12].

$$G_{DS} = 965\, f_{DS}^{-0.595}\, I^{-0.669} \qquad (1)$$

This relationship was developed for VAR of 430 mm diameter Inconel 718 electrodes and was found to be most accurate when applied to melting at furnace pressures below 10 mTorr. We use this relationship here knowing it may not be quantitatively correct for this size electrode, alloy, and particular furnace circuit (the circuit inductance maybe important).

The resulting ingots where sectioned lengthwise following melting. Prior to sectioning, the top flash (or crown) of about 75 mm was cut off for ease of handling. This flash was caused by a combination of small splashes due to bubbles of gas coming out of the melt and the large splash caused by the electrode dropping into the melt. The macrovoids in the sectioned ingots were filled with an epoxy and then the sections were polished. The polished ingot sections were then etched to reveal the grain structure.

Constant Current Melt

The first melt was performed with a constant current of 3700 A. The VAR controller was set to adjust the electrode gap so that a voltage of 23.35 V was maintained. Because voltage is not a particularly sensitive indicator of electrode gap, this mode of control is not expected to hold the electrode gap particularly well.

Prior to strike off, the vacuum was 3 mTorr with a leak rate of 0.4 mTorr/minute. Once melting began, gas evolving from the melt increased the pressure to around 60 mTorr. The bubbling of this gassy melt resulted in metal being splashed up onto the crucible walls creating a thick crown.

In Figure 2 the run chart for this melt is shown with the measured current, voltage, ram position, electrode mass, and drip-short frequency. Also plotted is the melt rate calculated as a 2 minute central average of the slope of the electrode mass (the average was not taken across the drop-in discontinuities) and the estimated electrode gap calculated from equation (1).

The melt rate begins to increase at 16 minutes into the melt. This corresponds to the point at which the thermal boundary layer, of approximately 85 mm, begins to impinge upon the thermal discontinuity of the weld.

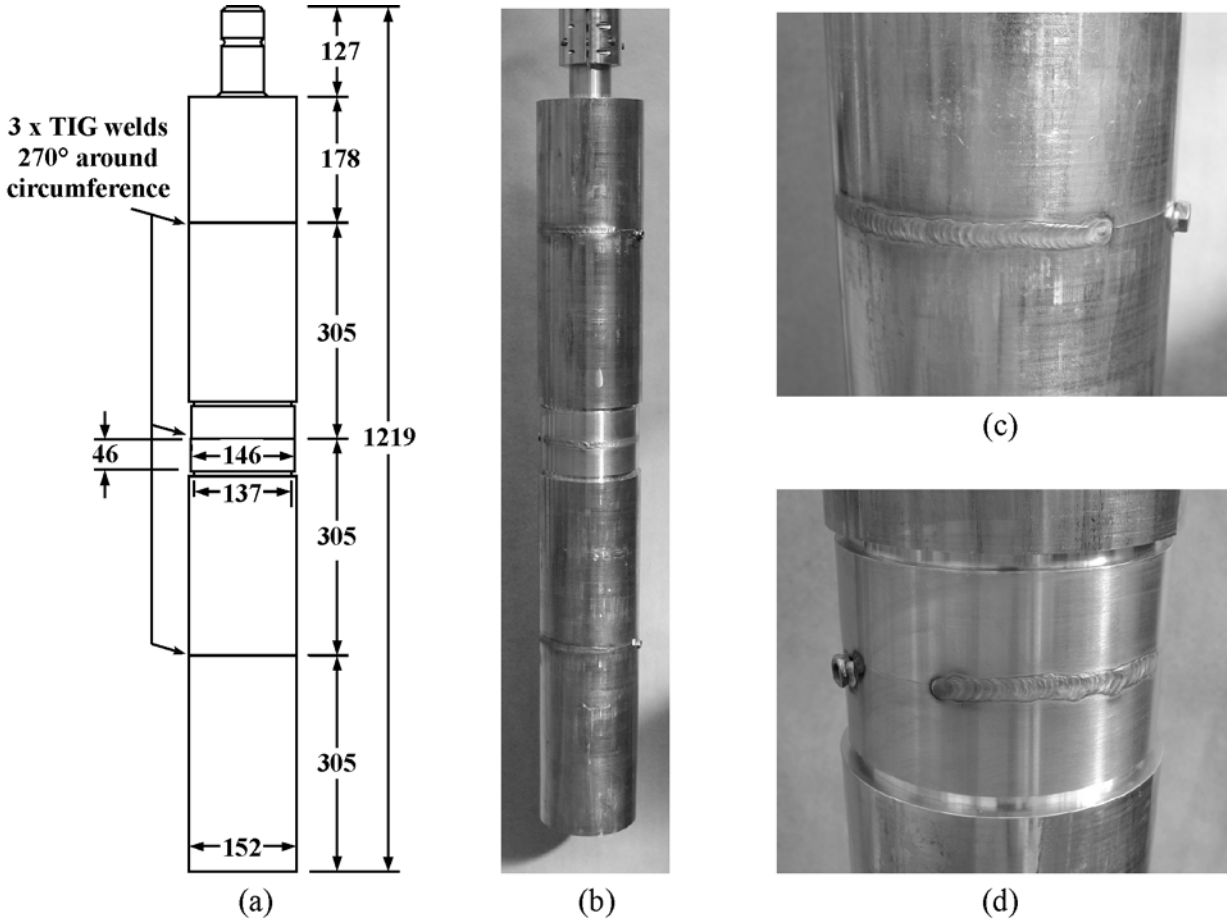

Figure 1: Segmented electrode used for experiments, (a) electrode dimensions in millimeters, (b) photograph of full electrode, (c) detail of top weld, and (d) detail of middle weld

Table 1: Times at which the welds are melted through causing a drop of electrode sections into the ingot. The weight loss from the load cell readings and the estimated gap are also given.

Heat	Time (min:sec)	Weight Loss (g)	Estimated Gap (mm)	Equivalent L (mm)*
Constant Current	21:22	3390	27	23
	40:20	3900	27	26
	59:06	4070	26	27
Melt Rate Control	21:37	2910	17	20
	42:47	2800	18	19
	62:31	4610	24	31

* Length of a right cylinder with the weight equivalent to the weight loss and with the same diameter as the electrode.

In Figure 3 an enlarged portion of the load cell output is shown. At 21 minutes and 22 seconds into the melt, the mass of the electrode drops by 3.4 kg. Because of the shallow depth of the welds and the convex electrode tip profile during melting, the welds melted through before the entire section had melted and the remaining portion dropped into the melt. Once the electrode tip falls in and the arc is in contact with the cool side of the weld the melt rate drops. The melt rate recovers over the next 4 minutes. The mass of the electrode tips that dropped in, and the corresponding elapsed time at which this occurred, are tabulated for all 3 segments in Table 1.

At 50 minutes and 26 seconds a gap check was performed by commanding the ram to drive in until a direct short occurred. Once the short occurred the ram was backed out 9 mm. From this travel the electrode gap was determined to be 46 mm, while the estimated gap given by equation (1) was 26 mm. Following this transient the ram drive rate decreased as the gap opened back up. The discrepancy between the measured (26 mm) and calculated gap (46mm), is likely due to a combination of (a) a poor correlation for this equation developed for the melting of large 718 electrodes and these small stainless steel electrodes, and (b) the high pressure of these melts (approximately 60 mTorr).

Once the top weld was melted through, and the corresponding change in the load cell was noted, melt current was turned off, the ram was backed off, and the ingot was allowed to cool.

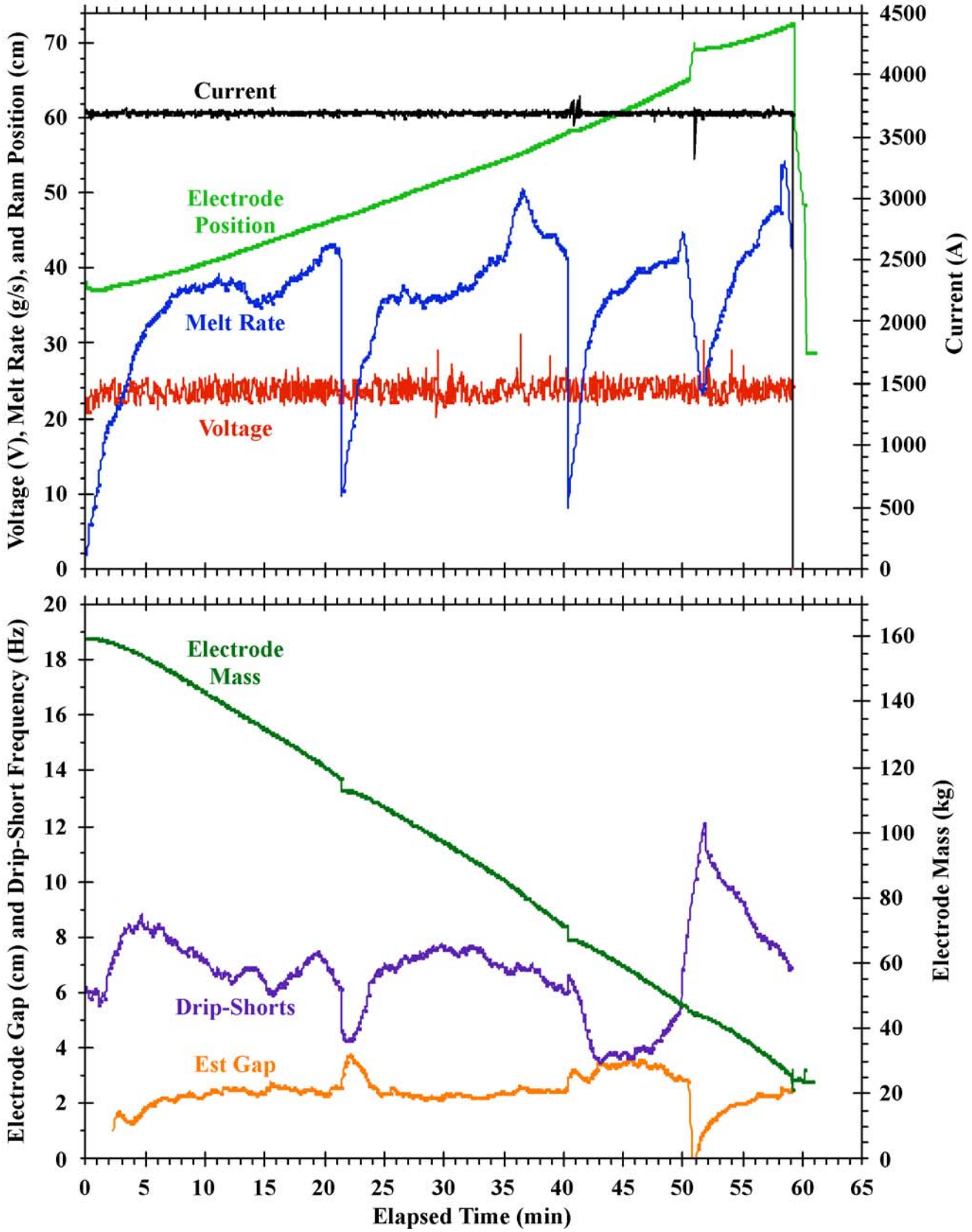

Figure 2: Run chart for constant current VAR of welded 304 stainless steel electrode.

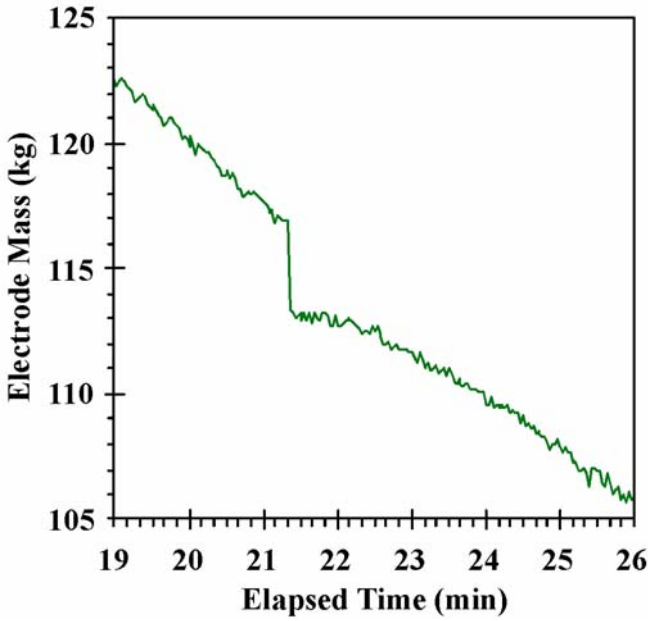

Figure 3: Detail of load cell output as weld melts though and electrode tip falls into the melt.

Melt Rate Controled Melt

The second melt was performed under melt rate control using the melt rate controller developed at Sandia National Laboratories and is described in detail elsewhere [8-9, 13]. As this controller was used for this experiment, the electrode gap was controlled by drip short frequency. Again due to dissolved gas in the electrode, splashing of metal up onto the crucible walls above the shelf occurred.

The run chart for this melt is shown in Figure 4. The commanded or reference electrode gap is shown in addition to the measured current, voltage, ram position, electrode mass, and drip-short frequency. As before, the melt rate is calculated as a 2 minute central average of the slope of the electrode mass (the average is not taken across the discontinuity) and the estimated electrode gap calculated from eqn. (1) are given.

The arc was struck at a current of 3800 A and the ram position was manually bumped down to maintain a tight electrode gap until melting began as indicated by the presence of drip shorts in the voltage. Control was handed off to the melt rate controller at 2 minutes into the melt. The melt rate controller was set for a nominal melt rate of 35 g/s and an electrode gap of 17 mm.

As shown in the run chart, Figure 4, there was an initial transient in the current and the ram position as the controller established the commanded melt rate and electrode gap.

As all three welds were approached the controller reduced current to maintain a constant melt rate. This reduction in current began at 16, 37, and 57 minutes for the first, second and third welds. These times corresponds to mass of approximately 12 kg remaining on the electrode sections. This is equivalent to 85 mm of running electrode length and is consistent with the estimated thermal boundary layer of 85 mm for these melting conditions.

As happened with the constant current melt, the weld melted through and an unmelted section of the electrode dropped into the melt. The mass of the electrode tip that dropped and the corresponding elapsed time at which this occurred is tabulated for all 3 segments in Table 1.

The controller interpreted the sequence of the weld melting through and the electrode fall off as an increase in melt rate. It responded by reducing the current even more; from 3300 to 2600 A over 40 seconds for this first event. This reduction in current and the much colder electrode face shut off melting. The controller then reacted to this cessation of melting by increasing current from 2600 to 3800 A over the next 60 seconds. This quickly brought the melt rate back up to the nominal 35 g/s. A similar transient occurred at the other two welds where the controller decreases the current to maintain a constant melt rate as the weld is approached and which is then followed by a rapid current increase to reestablish the commanded melt rate once the weld is melted through.

At 49 minutes and 20 seconds into the melt the electrode gap reference was ramped from 17 mm to 27 mm over a 1 minute interval. This wider gap was held for 200 seconds then reduced to 22 mm. These adjustments to the commanded gap were accommodated by the controller backing out the ram by 24 mm. The controller was able to maintain a constant melt rate throughout these adjustments to the gap.

Once the top weld was melted through, and the corresponding change in the load cell was noted, melt current was turned off, the ram was backed off, and the ingot was allowed to cool.

Results

Ingot Structure

The macroetched structures of the two ingots are shown in Figure 5. Three distinct interruptions can be seen where the columnar structure of the ingot is disrupted when the solid electrode tip dropped into and quenched the melt pool.

For the ingot melted under constant current conditions the wrought structure of the unmelted electrode tips are visible in Figure 5(a) as crescent shaped regions just above a layer of porosity. The unmelted tips have sunk to the bottom of the melt as would be expected from the greater density of the solid. The electrode piece from the first weld lies tilted at 9° from the horizontal. At the edges of the ingot, the columnar grain structure is able to continue to grow in from the sides across the first two disruptions. The columnar grain structure in the center of the ingot reestablishes itself from the quenched region. At the top of the ingot the last portion of the electrode to fall off sits inclined about 30° from the horizontal. There is a layer of liquid that has frozen on top of this layer. It appears that the electrode tip quenched most of the melt pool. The liquid in the pool did not have time to reform a horizontal surface prior to freezing after the tip splashed in.

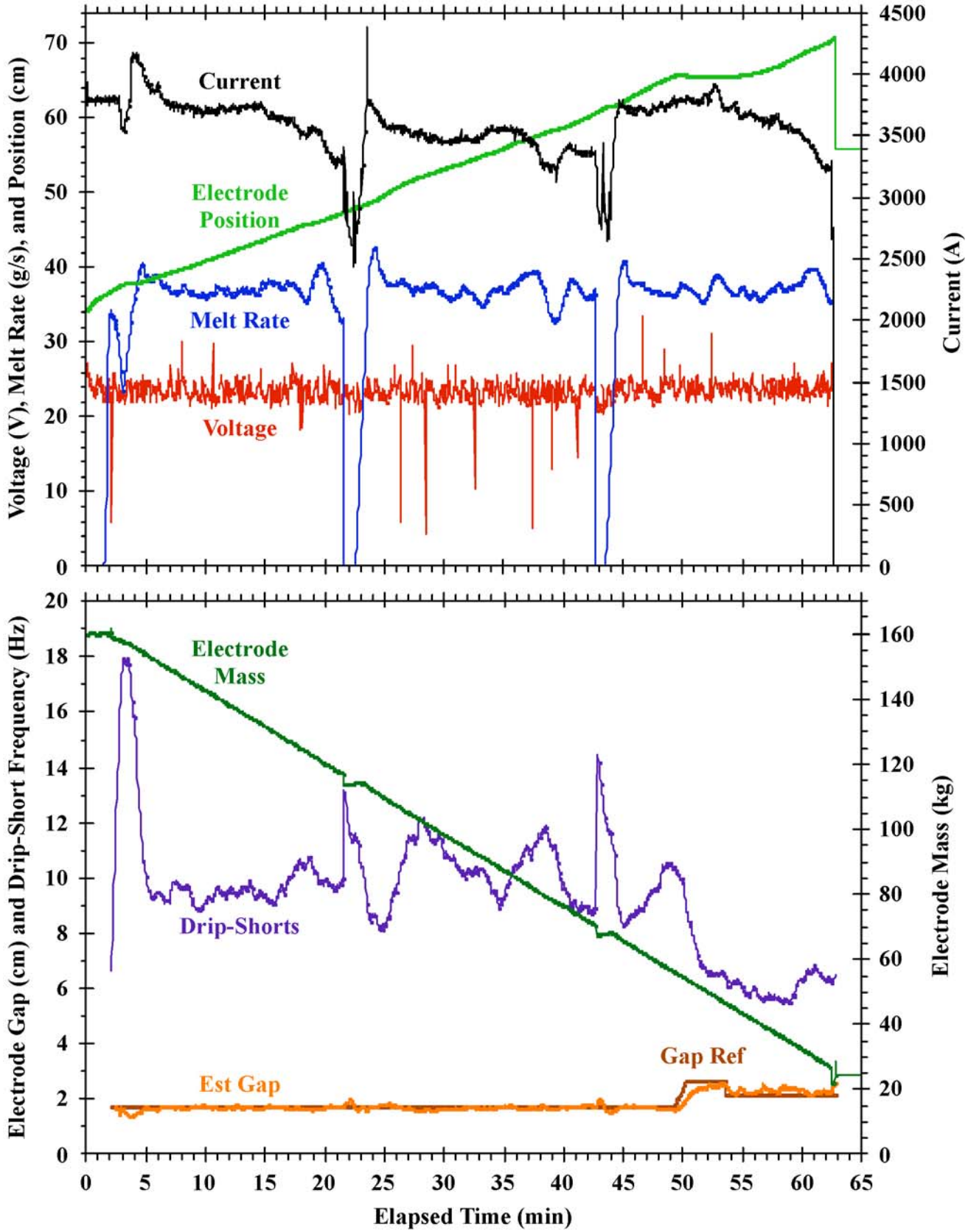

Figure 4: Run chart for melt rate controlled VAR of a welded 304 stainless steel electrode.

(a) (b)

Figure 5: Etched sections of final ingots, (a) constant current and (b) constant melt rate controlled.

The radius of the electrode tip remnants was measured from the sectioned ingot and was 92, 70, and 80 mm for the first, second and third drop-in events respectively. The true tip radius is not known because sectioning may not occur exactly thought the center of the electrode tip, but it is clear that the tips on these ingots were badly rounded at the time at which they dropped.

The ingot structure is shown in Figure 5(b) for the ingot melted under melt rate control. A discontinuity is visible where the first two welds were melted through. Unmelted electrode material and macroporosity are not visible. Although there is a disruption associated with the tip dropping into the melt, the columnar grain structure of the ingot appears to be continuous across the quenched region. This may indicate that the quenched pool was melted back in the minutes following the drop-in event or at minimum that the tips that dropped were melted.

For the top weldment, where melting was stopped as soon as the electrode tip dropped in, there is macroporosity present under an unmelted crescent of the electrode tip. There is also a layer of approximately 18 mm of liquid that solidified on top of the electrode tip after it dropped into the melt pool.

The mass of electrode that dropped from the first two welds during the constant melt rate melt is 25% less than the mass of electrode that dropped from the constant current heat (Table 1). This is because the melt rate controller was able to maintain a tighter electrode gap that resulted in a flatter electrode bottom. This in turn delayed when the weld melted through and reduced the mass of electrode that dropped. This trend did not apply to the third weld of the melt rate controlled heat because of the intentional opening of the gap at 49 minutes time. This wider gap caused rounding of the electrode tip resulting in an earlier melt though of the weld. This happened because opening the gap made the gap comparable in size to the annular distance between electrode and crucible. This has the effect of transferring additional arc activity to the electrode sides.

Solidification Modeling

The *BAR* code [14] was used to simulate the VAR process for these two melt conditions. The *BAR* code simulates the VAR process using a 2D axisymmetric model. It solves conservation equations for electric charge, mass, momentum, and energy. *BAR* employs sophisticated electromagnetic and thermal boundary conditions that are intended to capture the effects of the imperfect temperature-dependent contact of the VAR ingot with the walls of the crucible. In addition to simple contact heat transfer, the thermal model includes heat transfer via evaporation, radiation, and film cooling. A one-dimensional thermal model of the copper stool is employed to better capture thermal effects on the bottom face of the ingot during the initial transient.

To simulate the constant current heat, a constant current of 3690 A and voltage of 23.7 V was used, while the melt rate was chosen to closely follow the experimentally observed melt rate. To simulate the constant melt rate heat, a constant melt rate of 36.5 g/s and voltage of 23.5 V was used, while the current was chosen to closely follow the experimentally observed current.

In Figure 6 half of the etched ingot is shown beside the results of *BAR* simulation results for two melt control strategies. The temperature in the ingot is indicated at three times corresponding to times just before the electrode tips dropped. Overlaid on both the thermal profiles and the ingot images are isotherms for the liquidus and solidus (1672 and 1727 K). The general melt pool size and shape is predicted with a good agreement to the experiment. The match of the melt pool profile to the microstructures are not perfect, in part since the *BAR* simulation does not account for the drop-in of the electrode tips. The mushy zone for these melts is quite small and is on the order of 10 mm throughout the melt schedule. Since the overall melt parameters were chosen to be similar, it is not surprising that differences in melt control strategy does not result in large differences in the melt pool shape or size predicted by *BAR*. *BAR* does not account for the rounding of the electrode tip due to the large electrode gap and small electrode-crucible annulus, and as such the partitioning of energy between the ingot and wall may be inaccurate for these conditions.

Discussion

The difference in the presence or lack of unmelted electrode in these two ingots could be due to several factors: (a) the mass of electrode that dropped, (b) the enthalpy of the melt pool just prior to the electrode tip dropping, and (c) the amount of power input following the drop.

The *BAR* simulation results were used to quantify the degree to which the dropped-in electrode tips cooled or quenched the molten metal pool. The temperature of the liquid pool predicted by *BAR*, just prior to each drop-in event, was used to calculate the enthalpy for each cell of the mesh. The enthalpy for each cell above the liquidus temperature was multiplied by the mass of each cell and was integrated to determine the total enthalpy of the pool. In addition, the mass of all the cells at or above the liquidus temperature was integrated to determine the total melt pool mass. These results are shown in Table 2.

Assuming that the dropped-in electrode and melt pool can be treated as an adiabatic system (over a short period of time) the enthalpies and masses were added to determine a combined pool-electrode enthalpy per unit mass. From this combined enthalpy the equilibrium temperature of the pool-electrode system was calculated. For simplicity the dropped electrode tip was assumed to be at the solidus temperature prior to dropping (this an upper limit). As shown in Table 2, the equilibrium temperature is between the solidus and liquidus for all 6 drop-in events. This analysis suggests that despite the differences in the mass of the electrode and the enthalpy of the melt pool, differences in the thermal conditions just after the electrode drops in are not sufficient to explain the presence or lack of unmelted electrode observed in the ingot. This analysis

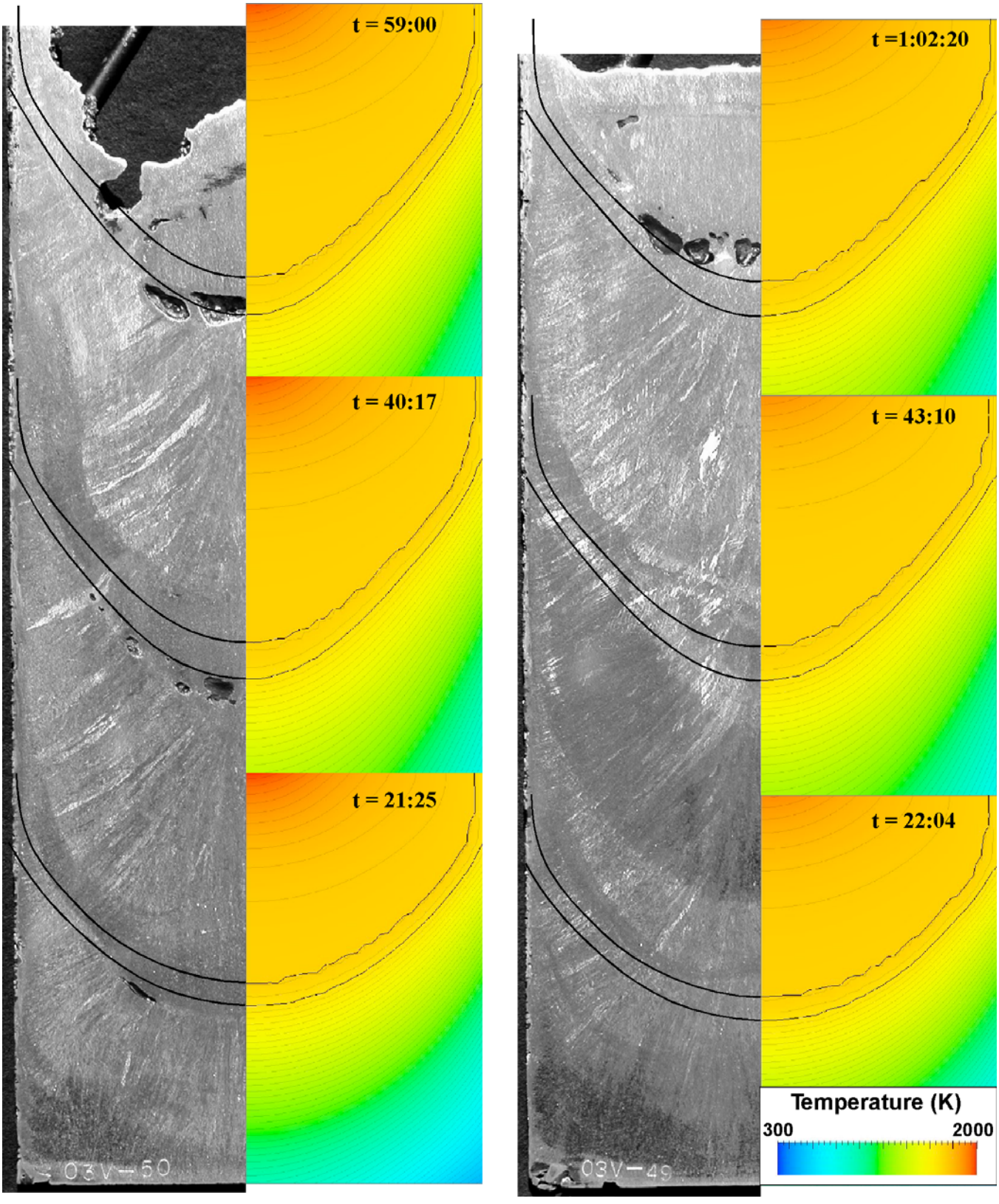

(a) (b)

Figure 6: Etched sections of ingots with thermal profile calculated to occur just prior to drop in events; (a) constant current and (b) constant melt rate controlled. Black lines on the thermal profiles and ingots are predicted solidus and liquidus lines.

Table 2: Comparison of the mass of the melt pool and enthalpy as determined by from the BAR simulation with the mass of electrode that dropped and it's enthalpy. For 304 stainless steel the solidus is 1673K and the liquidus is 1727K.

Melt	Time (min:sec)	Max. Pool Temperature (K)	Liquid Pool Mass (g)	Pool Enthalpy (MJ)	Electrode Tip Mass (g)	Electrode Enthalpy (MJ)	Combined Pool+Electrode Enthalpy (J/g)	Equilibrium Temperature (K)
Constant Current	21:22	1999	15932	21.65	3390	3.40	1296	1677
	40:20	1984	18706	25.35	3900	3.91	1295	1721
	59:06	1748	19643	26.29	4070	4.09	1281	1719
Melt Rate Control	21:37	1905	15154	20.49	2910	2.92	1296	1721
	42:47	1897	17660	23.83	2800	2.81	1302	1722
	62:31	1927	18068	24.42	4610	4.63	1281	1718

does not account for the fact that the kinetics of thermal equilibrium between the melt and electrode tip will be affected by the size and shape of the tip that drops.

This suggests that the lack of unmelted electrode observed in the melt rate controlled ingot may be due to the current increase following the drop-in event. Further work would be needed to confirm this conjecture.

Summary and Conclusions

These experiments show that VAR of segmented electrodes results in large melt and ingot microstructure transients. There is also the likelihood for sections of unmelted electrode and regions of large voids in the resulting ingots.

The melt rate controller was able to maintain a nearly constant melt rate though the perturbations caused by the segmented electrode.

Active control of melt rate may yield significant improvement in ingot properties when melting segmented electrodes where the potential exists for fall-in of unmelted electrode material.

Acknowledgements

The portions of work carried out at Los Alamos National Laboratory were supported by the United States Department of Energy under Contract W-7405-ENG-36. Los Alamos National Laboratory is operated by The University of California for the United States Department of Energy. The portions of this work carried out at Sandia National Laboratories were supported by the United States Department of Energy under Contract DE-AC04-94AL85000. Sandia National Laboratories is a multiprogram laboratory operated by Sandia Corporation, a Lockheed Martin Company, for the United States Department of Energy. Additional support for development of the melt rate controller was provided by the Specialty Metals Processing Consortium.

References

1. F. J. Zanner, Met. Trans. B, 10B, 133-142 (1979).
2. J. A. Van Den Avyle, J. A. Brooks, and A. C. Powell, JOM, 50, 22-25 (1998).
3. T. Suzuki, T. Shibata, K. Morita, T. Taketsuru, D. G. Evans and W. Yang, in *Proc. 2001 Int. Symp. on Liquid Metal Processing and Casting*, A. Mitchell and J. A. Van Den Avyle ed., AVS, NY, NY, p. 325, (2001).
4. B. K. Damkroger, J. B. Kelly, M. E. Schlienger, J. A. Van Den Avyle, R. L. Williamson, and F. J. Zanner, *Proc. Int'l. Symp. on Superalloys 718, 625, 706 and Varioius Derivatives*, E. A. Loria, ed. TMS, Warrendale, PA, pp. 125-135 (1994)
5. L. A. Bertram, J . Brooks, D. G. Evans, A. Patel, J. A. Van Den Avyle and D. D. Wegman, in *Proc. 1999 Int. Symp. on Liquid Metal Processing and Casting*, A. Mitchell, L. Ridgeway and M. Baldwin ed., AVS, NY, NY, p. 156 (1999).
6. X. Wang, M. D. Barratt, R. M. Ward, and M. H. Jacobs, J. Materials Science, 39, 7169 (2004).
7. X. Xu, R. M. Ward, M. H. Jacobs, P D. Lee, and M . McLean, *Met. Mat. Trans.* A; 33A, 1795-1804 (2002).
8. L. A. Bertram, R. L. Williamson, D. K. Melgaard, J. J. Beaman and D. G. Evans, U.S. Patent 6,115,404, Sept. 5, 2000.
9. J. J. Beaman, R. L. Williamson and D. K. Melgaard, in *Proc. Int. Symp. on Liquid Metal Processing and Casting*, A. Mitchell and J. A. Van Den Avyle ed., AVS, NY, NY, p. 161 (2001).
10. R. L. Williamson, J. J. Beaman, D. K. Melgaard, G. J. Shelmidine, A. D. Patel, and C. B. Adasczik, *J. Mater. Sci.*, 39, 7161 (2004).
11. R. L. Williamson, J. J. Beaman, D. K. Melgaard, G. J. Shelmidine, and R. Morrison, *Met. Mat. Trans.* B; 35B, 100 (2004).
12. R. L. Williamson, F . J . Zanner and S . M. Grose, *Met. Mat. Trans.* B, 28B 841 (1997).
13. R. L. Williamson, J. J. Beaman, and D. K. Melgaard, *Modeling, Control and Optimization in Ferrous and Nonferrous Industry Symposium*, ed. F. Kongoli, and B. Thomas, and K. Sawamiphakdi, The Iron and Steel Soc. and TMS, p. 209 (2003).
14. L. A. Bertram, C. B. Adasczik, D. G. Evans, R. S. Minisandram, P.A. Sackinger, D. D. Wegman, and R. L. Williamson, *Proc. 1997 Int. Symp. on Liquid Metal Processing and Casting*, A. Mitchell and P. Auburtin ed., AVS, NY, NY, p. 110 (1997).